

## The new materials processing beamline at the SRS Daresbury, MPW6.2

R. J. Cernik,<sup>a,b,c\*</sup> P. Barnes,<sup>b</sup> G. Bushnell-Wye,<sup>a</sup>  
A. J. Dent,<sup>a,‡</sup> G. P. Diakun,<sup>a</sup> J. V. Flaherty,<sup>a</sup>  
G. N. Greaves,<sup>d</sup> E. L. Heeley,<sup>e</sup> W. Helsby,<sup>a</sup>  
S. D. M. Jacques,<sup>b</sup> J. Kay,<sup>a</sup> T. Rayment,<sup>f</sup>  
A. Ryan,<sup>e</sup> C. C. Tang<sup>a</sup> and N. J. Terrill<sup>a</sup>

<sup>a</sup>Daresbury Laboratory, Warrington WA4 4AD, UK, <sup>b</sup>Department of Crystallography, Birkbeck College, London WC1E 7HX, UK, <sup>c</sup>Manchester Materials Science Centre, University of Manchester and UMIST, Grosvenor Street, Manchester M1 7HS, UK, <sup>d</sup>Department of Physics, The University of Wales, Aberystwyth, Penglais, Aberystwyth, Ceredigion SY23 3BZ, UK, <sup>e</sup>Department of Chemistry, University of Sheffield, Western Bank, Sheffield S10 2TN, UK, and <sup>f</sup>Department of Chemistry, University of Cambridge, Cambridge CB2 1TN, UK.  
E-mail: r.j.cernik@dl.ac.uk

A new beamline (MPW6.2) has been designed and built for the study of materials during processing where three synchrotron techniques, SAXS, WAXS and XAS, are available simultaneously. It has been demonstrated that Rietveld refinable data can be collected from silicon SRM 640b over a 60° range in a time scale of 1 s. The data have been refined to a  $\chi^2$  of 2.4, the peaks fitting best to a Pearson VII function or with fundamental parameters. The peak halfwidths have been found to be approximately constant at 0.06° over a 120° angular range indicating that the instrumental resolution function has matched its design specification. A quantitative comparison of data sets collected on the same isotactic polypropylene system on MPW6.2 and DUBBLE at the ESRF shows a 17% improvement in angular resolution and a 1.8 improvement in peak-to-background ratio with the RAPID2 system; the ESRF data vary more smoothly across detector channels. The time-dependent wide-angle XRD was tested by comparing a hydration reaction of gypsum–bassanite–anhydrite with energy-dispersive data collected on the same system on the same time scale. Three sample data sets from the reaction were selected for analysis and gave an average  $\chi^2$  of 3.8. The Rietveld-refined lattice parameters are a good match with published values and the corresponding errors show a mean value of  $3.3 \times 10^{-4}$ . The data have also been analysed by the Pawley decomposition phase-modelling technique demonstrating the ability of the station to quickly and accurately identify new phases. The combined SAXS/WAXS capability of the station was tested with the crystallization and spinodal decomposition of a very dilute polymer system. Our measurements show that the crystallization of a high-density copolymer (E76B38) as low as 0.5% by weight can be observed in solution in hexane. The WAXS and SAXS data sets were collected on the same time scale. The SAXS detector was calibrated using a collagen sample that gave 30 orders of diffraction in 1 s of data collection. The combined XRD and XAS measurement capability of the station was tested by observing the collapse and re-crystallization of zinc-exchanged zeolite A (zeolite Zn/Na-A). Previous studies of this material on station 9.3 at the SRS were compared with those from the new station. A time improvement of 38 was observed with better

quality counting statistics. The improved angular resolution from the WAXS detector enabled new peaks to be identified.

**Keywords:** X-ray instrumentation; detector development.

### 1. Introduction

#### 1.1. Scientific objectives of the beamline

We report on the design, construction and early commissioning tests of a new beamline (MPW6.2) on the SRS Daresbury that is dedicated to the study of materials processing. This new beamline was funded by the Engineering and Physical Science Research Council in May 1999 and received its first light in January 2002. The scientific philosophy behind the new development is to study materials as they are synthesized, processed or otherwise transformed. The ultimate goal of the proposed experiments is to directly correlate the microscopic structure of the material with its macroscopic physical properties. The main synchrotron techniques available on the new station are very fast powder diffraction (XRD) or wide-angle scattering (WAXS), small-angle scattering (SAXS) and X-ray absorption spectroscopy (XAS). The major detector development has been in the area of fast powder diffraction that has previously been the rate-limiting step when studying solid-state processes. The experimental area has been designed so that very large equipment can be installed to utilize the X-ray beam. Any one, or all, of the three main synchrotron radiation techniques can be combined with direct measurements of the physical properties of the sample in real time. Combined experiments have been limited in the past by the speed of the WAXS. The new station has been designed to collect the WAXS data on the same time scales of milliseconds to minutes as the SAXS or XAFS data. This is nowhere near the ultimate data-collection rate available on modern synchrotron sources where femtosecond slicing is possible. However, the new station's data-collection rates are very well suited to the study of solid-state reactions while delivering data suitable for structural refinement.

The idea of combining synchrotron X-ray techniques to study changing systems is certainly not new. Couves *et al.* (1991) showed how the catalyst precursor aurichalcite converted to catalytically active Cu and ZnO. They used energy-dispersive EXAFS (EDE) together with an INEL curved position-sensitive detector (PSD) to collect the diffraction data. The drawbacks with this method were that the diffraction pattern could only be recorded with sufficient statistical precision in tens of minutes and that the EDE cannot be easily switched between edges further apart than 1000 eV. In addition, the spatial resolution and total count rate of the INEL PSD are too low to carry out anything other than phase identification on a sub-second time scale. The problem of tunability was partially solved using combined quick EXAFS (QuEXAFS) and XRD (Sankar *et al.*, 1993) where cordierite was synthesized from a precursor zeolite. Again the diffraction data collection was the limiting factor and did not deliver data of a sufficiently high quality to permit a quantitative Rietveld refinement. In the area of soft materials processing (*e.g.* polypropylene), very high count rates and strong texture are encountered which make accurate diffraction data collection even more challenging. Terrill *et al.* (1998) solved this problem by recording the diffraction patterns using an image-plate detector (IP). The corresponding SAXS pattern was recorded using a two-dimensional gas chamber and the polymer was extruded *in situ* using a laboratory-scale single-screw extruder. The use of the IP reduces data-collection times and provides texture information; however, it cannot be read out in real time and cannot give genuinely simulta-

‡ Present address: Diamond Light Source Ltd, Chilton, Didcot, Oxon OX11 0QX, UK.

neous read out with the SAXS. The same group subsequently used two two-dimensional gas chambers to reveal real-time information on the pre-crystallization of the polymer system (Olmsted *et al.*, 1998).

By using the technique of energy-dispersive diffraction (EDD) data can be collected on a sub-second time scale; the technique is also well suited to samples in hostile environments. Colston *et al.* (1998) studied the transformation of cements undergoing high-temperature hydration. They used a three-element solid-state detector to partially solve the energy-dispersive data-collection problems such as limited data range, sample gauge volumes and spectral matching. However, the EDD technique is ultimately limited by the energy resolution of the solid-state detector ( $\delta E/E \approx 2\%$ ). In practice, the data from EDD cannot be refined in a satisfactory way and does not give accurate atomic coordinates. To date, its use has largely been confined to studying the kinetics and identification of phase transitions.

### 1.2. Design rationale

The examples listed above illustrate some of the experimental problems that led to the design specification for the new beamline. The specification for the XRD component of MPW6.2 was to maintain the speeds inherent in the EDD technique but with high angular resolution using monochromatic X-rays to produce data suitable for Reitveld refinement. In addition, the WAXS component of the beamline has been designed so that data can be collected in the same registered time frame as the SAXS data in order to ensure genuinely simultaneous data collection. The SAXS detector required less improvement in performance since the low-angle data can be collected typically two orders of magnitude faster than the WAXS. The monochromator system has been designed to be very stable and rapidly tunable over a wide energy range from 5 to 18 keV to cater for QuEXAFS (Cheung *et al.*, 1999). The sample environment space is sufficiently large ( $\sim 1\text{ m}^3$ ) to accommodate large-scale plant equipment such as polymer extruders, crystallization equipment, furnaces, cryostats and other environmental chambers. The station has been built with a great deal of flexibility in the experimental services and software to accommodate a wide range of direct physical measurements. It is well known that EDD data can be collected in milliseconds; however, this is a white-beam technique. In order to carry out monochromatic studies on the same time scale the X-ray flux has to be significantly increased.

The WAXS detection system has been designed to cope with a count rate of  $\sim 10^7$  Hz, a  $60^\circ$   $2\theta$  range and an angular resolution such that a single peak with no inherent sample broadening will have a halfwidth of  $0.06^\circ$ . The SAXS detection system is connected to the same instrumentation cabinet and the same electronic architecture to ensure very rapid simultaneous data collection. The following section describes in more detail the essential elements of the new station.

## 2. Beamline design

### 2.1. X-ray delivery

The SRS straight section number 6 has been adapted with a 20 mm external gap vessel capable of accommodating an insertion device of length 1 m. In order to produce the necessary X-ray flux, a ten-pole wiggler has been installed that is identical in design to that installed on beamline 14 and described by Duke *et al.* (1998). The X-ray flux output of this device reaches a peak at approximately 8 keV. This has been measured, using a silicon analogue photodiode, at  $4 \times 10^{12}$  photons  $\text{s}^{-1}$  into the focal spot ( $1\text{ mm} \times 2\text{ mm}$ ). This is a factor of 1.4 lower than that calculated, the difference being assigned to sub-optimal beam steering at the time of measurement. The beryllium window absorption at low energy and the high-energy flux

limit from the 2 T magnetic poles of the insertion device define the practical photon energy range available (5 to 18 keV). The flux from the new insertion device becomes equivalent to that of the two existing SRS high-magnetic-field wavelength shifters (5 and 6 T) on beamlines 9 and 16 at an energy of approximately 20 keV. The maximum deflection of the electron beam as it passes through the magnet is 500  $\mu\text{m}$ ; this is smaller than the electron beam dimension and so does not significantly contribute to the source size. Fig. 1 shows the magnetic field strength for the new multipole wiggler plotted against the horizontal viewing angle (Laundy, 1999). It can be seen that the maximum field strength coincides with the centre of the fan. While this is true for the emitted radiation observed directly down the source centre line, it is not the case as the observation point is moved in either direction. At angles away from the centre of the fan the tangent points away from the centre of the poles and the magnetic field at the tangent point falls. This results in a drop in flux and a movement of  $\lambda_c$  as a function of angle. It can be seen that there is no flux beyond  $\pm 7.5$  mrad. The flux towards the edge of the fan becomes quite soft and a practical X-ray cut-off is reached at approximately  $\pm 5$  mrad. Fig. 2 shows the flux at various energies across the fan. The attenuation of the X-ray flux at higher energies becomes greater as a function of angle from the centre of the fan.

The total radiation fan from the multipole wiggler on beamline 6 is split into two sections 9.8 m from the tangent point. A plane mirror deflects 7.5 mrad of beam in the UV energy range for use in station MPW6.1 (Bowler *et al.*, 2002). The optical design of the splitter presented a considerable engineering challenge to accommodate the

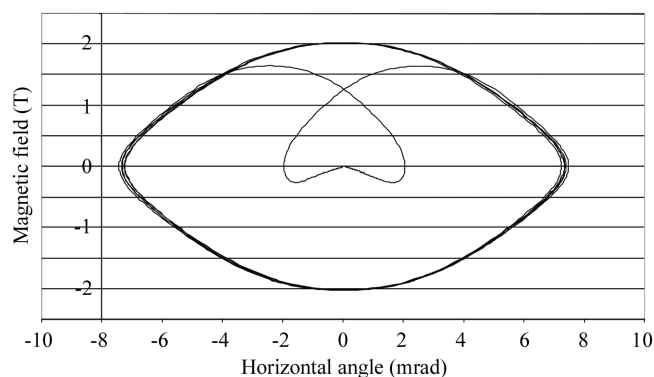


**Figure 1**  
Diagram of the magnetic field strength against distance from the beam centre. It can be seen that the X-ray flux falls to unacceptably low levels beyond 4 mrad from the beamline centre.

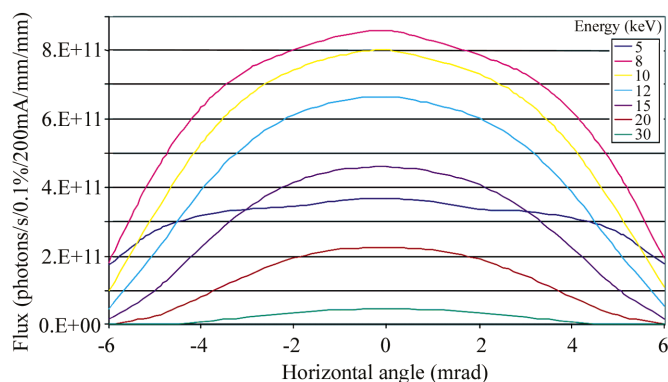


**Figure 2**  
Flux at different energies across the available MPW6 fan.

UV mirrors and the X-ray beam definition that required building the largest UHV vessel on the SRS to date. The UV mirrors are protected from the lower vacuum X-ray line by residual gas analysers and a 0.75 mm-thick water-cooled beryllium window. The X-ray beam passes the first UV mirror from the centre of the fan out to the practical cut-off for the source, 7.5 mrad from the centre line. The first beamline element specific to MPW6.2 is a water-cooled defining aperture at 12.88 m that defines an X-ray beam divergence of 4.5 mrad (horizontal) and 1.4 mrad (vertical). This is followed by the first set of water-cooled slits. The first of two identical planar cylindrically bent Si mirrors (1200 mm × 120 mm × 50 mm with a 500 Å rhodium coating) has been bent to a radius of 8243 m to achieve a vertically parallel beam. The first mirror provides a collimated beam onto the two-crystal monochromator of the design described by Dobson *et al.* (2002). The monochromator has a flat water-cooled first crystal cut along the [111] direction. This crystal is 15.98 m from the tangent point. The second crystal is sagittally bent and collects the entire available horizontal aperture. The crystal can be bent dynamically during spectroscopy scans reliably and reproducibly. The bent Si crystal is also cut along the [111] direction and has four ribs to prevent anticlastic bending. The focal point of the second crystal can be adjusted to any point in the experimental area over a range of 5 m. The monochromator is the only means of horizontal focusing. A second set of slits immediately after the monochromator provides further beam definition. The second Si mirror provides a vertical line of approximately 100 µm with a bend radius of 1551 m. The third set of slits follows the second mirror and is followed by the station stop. The monochromator mirror systems are all contained within a separate optics hutch in order to reduce parasitic scattering.

## 2.2. Experimental hutch

The experimental hutch has a floor space of approximately 18.5 m<sup>2</sup> with a maximum usable length of 6 m. This has been designed to accommodate large items of experimental equipment including a 4 m small-angle-scattering camera. The first element of the experimental hutch is a pair of horizontal and vertical slits and a 0.9 mm-thick second beryllium window at 20.665 m. This point marks the beginning of user-specified equipment. For SAXS and SAXS/WAXS experiments a mica window fitted to an extension pipe that ends at the sample position can replace this window.

A Huber two-circle diffractometer has been designed and built to house sample environments up to a maximum weight of 20–30 kg and with a usable space of approximately 300 mm × 300 mm × 300 mm. Sample environments larger than this can be accommodated by moving the whole diffractometer away leaving a usable space of approximately 8 m<sup>3</sup>. The 2θ axis of the diffractometer has been designed using finite-element analysis to support a weight of 40 kg specifically to accommodate the curved position-sensitive detector for powder data collection.

## 2.3. Detectors

The station has been equipped with a combination of small- and wide-angle detectors that can cope with the very high count rates and short data-collection times associated with materials processing applications. The detectors have also been constructed with good spatial resolution in order to obtain quantitatively significant data. A second generation of the RAPID readout electronics (Berry *et al.*, 2002) has been built for the dual one-dimensional small-angle detector (RAPID SAXS) and the wide-angle-scattering X-ray detection system (RAPID2). The ADC per channel system is designed to interpolate and yields typically 32 pixels per channel. The

wide-angle detector uses 128 channels of electronics to produce 4096 pixels with a full width at half-maximum (FWHM) of 4 pixels, *i.e.* the ability to resolve 1024 peaks across the detector. This corresponds to a FWHM of approximately 400 µm over a 384 mm-long (60°) curved detector. A powder sample with small intrinsic line broadening would be recorded with a peak halfwidth of approximately 0.06°. This is far from the highest resolution that can be obtained using powder diffraction (for example, see Masson *et al.*, 2001). However, the majority of samples used for dynamic processing will be encapsulated in specialist environmental cells where the beam footprint will be a significant part of the instrumental resolution function. The choice of spatial resolution was a compromise between the desire to collect HRPD for Reitveld refinement and the need to measure samples in realistic situations. A second group of 128 channels was built to instrument the 200 mm-radius quadrant detector for simultaneous small-angle-scattering measurements. The system performance has been designed to cope with over 20 million events per second for each wire.

The remainder of the hutch space has been configured in a modular fashion so that a variety of configurations and direct physical measurements can be carried out on the sample as it is processed. These techniques could include Raman spectroscopy, DC and AC conductivity, DSC, dielectric resonance properties or resistance. The hutch has been designed to accommodate lasers for heating, sample cells to produce high pressures and high temperatures, or both. The station software has been written so that any of these measurements can be integrated and time-stamped simultaneously with the diffraction, EXAFS or small-angle scattering.

## 3. Station commissioning trials

### 3.1. RAPID2 calibration using silicon SRM 6340b

Data were collected from a silicon standard reference sample (SRM 640b) at a wavelength 0.128 nm using RAPID2. The detector instrumental resolution function was measured by stepping RAPID2 on the 2θ axis of the diffractometer at very fine steps through the Si diffraction peaks. Every part along the active length of the RAPID2 detector measured at least one peak and many parts of the detector measured up to ten reflections. In this way a calibration file was built up that was stored and subsequently used to obtain the gain and spatial-resolution parameters for the RAPID2 system. The full calibration was undertaken using 0.5 mrad steps resulting in 2094 data sets. Table 1 shows the results from 11 of those data sets spaced at approximately 5° intervals. The mean position, intensity, peak half width and Lorentzian component of the pseudo-Voigt shape are given, together with their standard deviations. The variation of intensity from region to region has been found to be comparable with the statistical errors expected from the Poisson distribution. Fig. 3 shows the superposition of six measurements of the 400 reflection at different detector positions; under ideal circumstances these would be identical to within Poisson counting statistics. Table 1 shows that the intensity reproducibility is of this order.

The positional errors occur in the third decimal place with some exceptions directly over a channel. These over-channel anomalies are proportional to the detector gain and a route to removing them completely has been developed. Details of the over-channel anomalies together with a detailed account of the design of RAPID2 and its calibration procedures will be published shortly (Cernik, 2004). Fig. 4 shows a full Rietveld refinement of one of the silicon data sets; all data sets yield similar results. This is a severe test of the detector performance since the only variables are the 2θ zero error, size and shape fundamental parameters and the temperature factor.

**Table 1**  
Comparison of silicon peak parameters measured on the RAPID2 detector.

$2\theta$ ( $^\circ$ )	$2\theta$ error ( $^\circ$ )	Intensity	Intensity error	Poisson intensity error	FWHM ( $^\circ$ )	FWHM error ( $^\circ$ )	Lorentz component	Lorentz component error
39.02904	0.003504	5157.667	77.73245	71.8169	0.05582	0.00778	0.307333	0.053107
46.13272	0.003647	3334	31.84337	57.7408	0.067968	0.009634	0.35175	0.084326
56.40016	0.001762	973.5	9.246621	31.20096	0.07125	0.00465	0.365	0.066597
61.99215	0.00274	1580.143	53.66386	39.75101	0.070969	0.008762	0.35119	0.069247
70.73173	0.003614	2174.375	55.62871	46.63019	0.068351	0.006724	0.422125	0.077024
75.74752	0.010786	1222.667	34.56516	34.96665	0.065829	0.005135	0.474785	0.092471
83.87695	0.00732	659.8	27.43801	25.68657	0.07765	0.009303	0.3599	0.17791
88.68661	0.007259	1162	37.9638	34.08812	0.0795	0.011314	0.425111	0.094803
96.69378	0.00691	947.125	28.3571	30.7754	0.07345	0.006393	0.53225	0.072592
101.5532	0.006018	428.1429	20.30951	20.69161	0.070157	0.002674	0.659429	0.163221
109.8662	0.006383	383	21.9545	19.57039	0.06456	0.003223	0.95	0.01234
115.0528	0.005437	653.2	22.34278	25.55778	0.0776	0.007125	0.5366	0.078309
124.2592	0.003323	1213	20.29778	34.82815	0.071467	0.001168	0.732667	0.015948
130.2921	0.000877	1072	11.31371	32.74141	0.07775	0.000212	0.999	0.001414

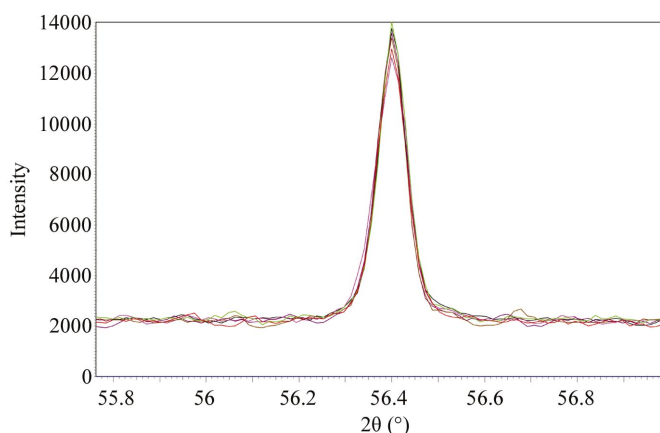


**Figure 3**  
A plot of six superimposed Si 400 peaks. Each peak was measured at a different point on the RAPID2 detector. They should ideally be identical. The variations of all observed reflections are given in Table 1.

Any detector distortions or inhomogeneities manifest themselves as asymmetric peak shapes (spatial distortion) or intensity variations (gain variations). The nature of the peak-shape variation with  $2\theta$  is shown in Fig. 5; the detector instrumental resolution function dominates the diffraction pattern, hence there is very little variation in halfwidths with  $2\theta$ . The contribution from the sample strain shows up as an increase in the Lorentzian component with increasing  $2\theta$ .

**3.2. The crystalline phase of isotactic monoclinic polypropylene**

The performance of RAPID2 was compared with the WAXS detector on DUBBLE at the ESRF. This is the only other dedicated SAXS/WAXS synchrotron user facility with an established and excellent track record of scientific output (Borsboom *et al.*, 1998). The wide-angle detector on DUBBLE is based on gas-glass microstrip technology. This has inherently higher count rates than RAPID2 but at present poorer angular resolution. Data were collected using the same isotactic monoclinic polypropylene system for 2000 s on MPW6.2 and for 3900 s on DUBBLE. The data were normalized to each other by use of the total integrated count rate in each pattern (Fig. 6). Pseudo-Voigt peaks were fitted to each main peak group and the results are presented in Table 2. The MPW6.2 data have better angular resolution (17%) and an improved peak-to-background ratio ( $\times 1.8$ ). Both data sets fit well to a monoclinic unit cell of  $a = 0.665$  (5),  $b = 2.066$  (5),  $c = 0.623$  (5) nm that agrees with

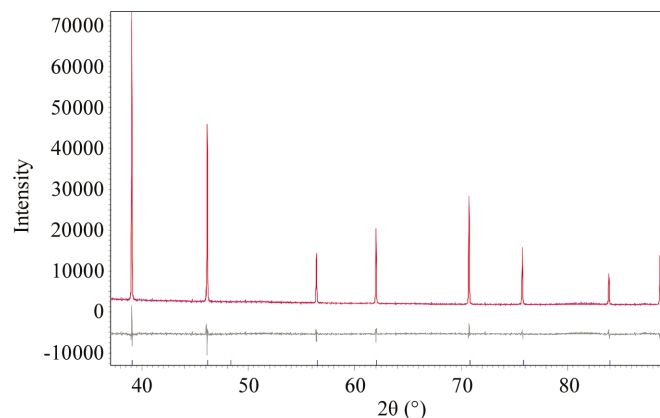


**Figure 4**  
A full Rietveld refinement of the Si diffraction pattern; the diffraction data were collected in 1 s.

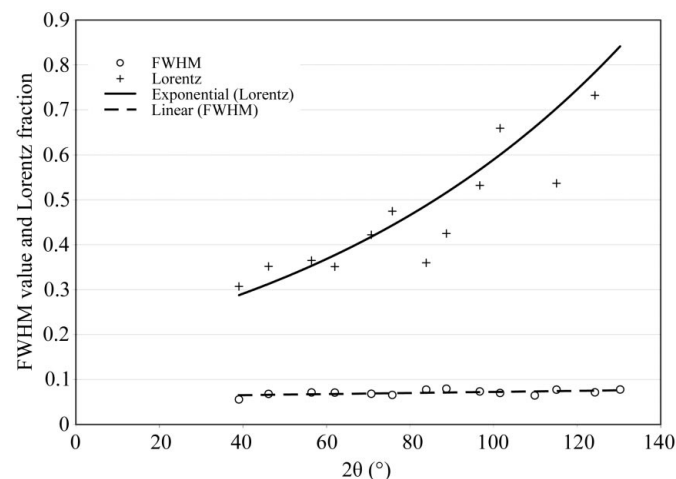


**Figure 5**  
A plot of the FWHM of Si SRM 640b with angle as measured on RAPID 2, together with the corresponding increase in Lorentzian fraction as fitted with a pseudo-Voigt function. The y scale for the peak halfwidth is in degrees and is unitless for the Lorentzian fraction.

previously published values. The data from DUBBLE have a smoother background and better low-angle shielding. The higher angular resolution of the RAPID2 detector lends itself well to the investigation of crystalline phases in polymer systems.

**Table 2**

Comparison of parameters from the same polyethylene sample measured on DUBBLE at ESRF and on MPW62 at Daresbury.

Peak position DUBBLE $2\theta$ ( $^\circ$ )	Peak position MPW6.2 $2\theta$ ( $^\circ$ )	Peak intensity DUBBLE	Peak intensity MPW 6.2	Lorentzian fraction DUBBLE	Lorentzian fraction MPW	FWHM DUBBLE ( $^\circ$ )	FWHM MPW6.2 ( $^\circ$ )	Ratio FWHM MPW6.2 : DUBBLE	Intensity ratio MPW6.2 : DUBBLE
12.71165	13.58995	42.1	78.9	1	0.99	0.27	0.18	1.5	1.87
15.37234	16.23384	29.50	55.4	0.03	0.72	0.37	0.38	0.97	1.87
16.91594	17.93703	17.9	37.2	1	0.99	0.26	0.21	1.23	2.07
19.59713	20.78800	4.47	34.1	0	0.15	0.35	0.34	1.02	7.62
20.26862	21.42558	16.7	44.3	0.5	0.65	0.46	0.41	1.12	2.65

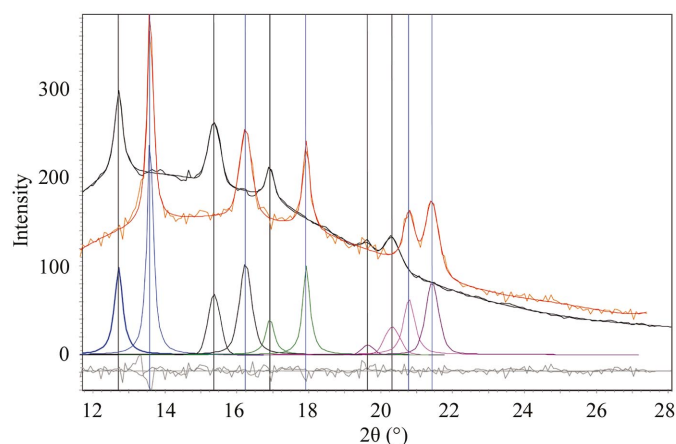


**Figure 6**

A comparison of the diffraction pattern of polypropylene collected at the ESRF (black curve) and on station 6.2 at Daresbury (red curve). The MPW6.2 data have higher angular resolution and higher integrated peak intensities. The gas–glass microstrip detector used at the ESRF does not suffer from the over-channel anomalies of RAPID2 and currently gives a smoother background.

### 3.3. The hydration reaction: gypsum–bassanite–anhydrite

The time-resolved XRD capability of the new facility was demonstrated using a known crystallographic transformation. The dehydration process of gypsum ( $\text{CaSO}_4 \cdot 2\text{H}_2\text{O}$ ) to bassanite ( $\text{CaSO}_4 \cdot 0.5\text{H}_2\text{O}$ ) and then to anhydrite ( $\text{CaSO}_4$ ) was chosen for this purpose. Previous studies have shown that the structure of gypsum is monoclinic; the first structure by Wooster (1936) gave  $a = 1.047$ ,  $b = 1.515$ ,  $c = 0.65$  nm,  $\beta = 151.55^\circ$ , space group  $C2/c$ . The first transformation takes place at  $T_N \approx 373$  K from the hydrated to the dehydrated structure, which is also monoclinic but with a different unit cell of  $a = 1.2062$ ,  $b = 1.266$ ,  $c = 0.693$  nm,  $\beta \approx 90^\circ$ . In our experiment, a horizontally focused and vertically collimated monochromatic beam of  $3 \text{ mm} \times 0.5 \text{ mm}$  was used ( $\lambda = 0.12$  nm). Fine gypsum powder loaded in a  $0.5$  mm-diameter glass capillary was placed inside a resistive furnace that was pre-adjusted to intercept the beam at the centre of the diffraction instrument. For dehydration, the sample was heated at a constant rate for less than 1 h, from ambient to temperatures ( $T \approx 573$  K) eventually around  $973$  K (*i.e.* well above  $T_N$ ). Structural changes were monitored by collecting diffraction patterns for 1 s every 3 s during heating. The gypsum–bassanite transformation observed is shown in Fig. 7(b) for 900 patterns centred about the transition point. Each pattern was collected for 3 s giving a total time of 2700 s for the set. Fig. 7(a) shows data from the same reaction studied on station 16.4 using energy-dispersive diffraction with 120 patterns collected over a total time of 2 h. Both data sets were collected using capillary geometry. It can be seen qualitatively from Figs. 7(a) and 7(b) that the monochromatic data extend twice as

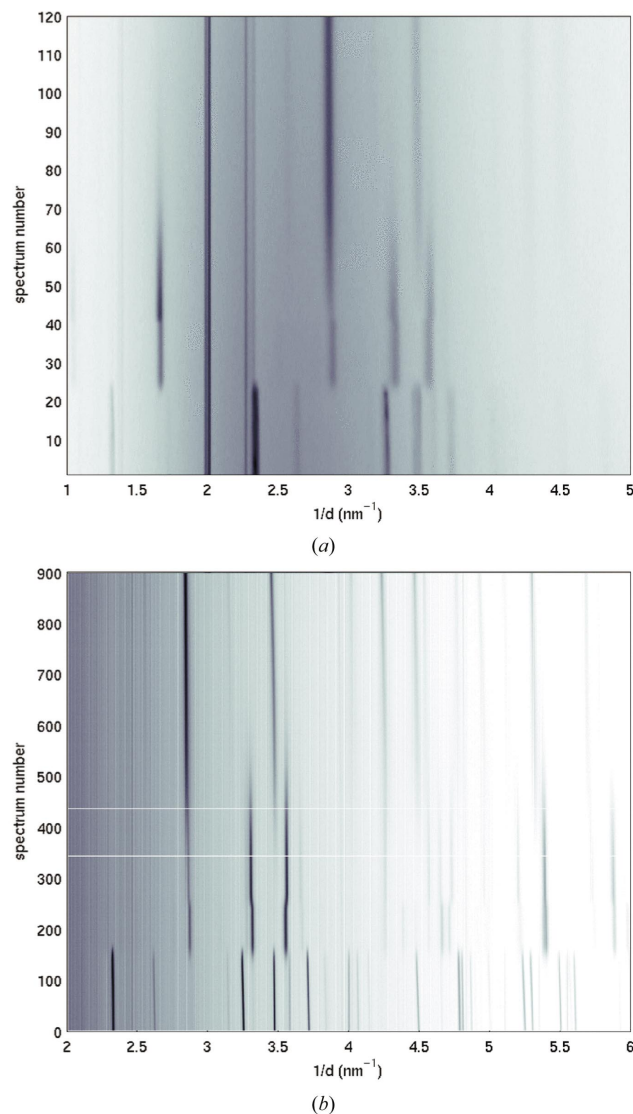


**Figure 7**

*x-y* plots of diffraction patterns versus time (frame number) showing the transformation of gypsum–bassanite–anhydrite. The sample temperature increases with frame number and the collection time for each frame is 1 s. Higher intensity is represented by darker shading. (a) Energy-dispersive data collected on station 16.4. (b) Monochromatic data collected on station 6.2. The data range and angular resolution are far superior with the monochromatic data. The MPW6.2 data were collected 1/3 faster than the energy-dispersive data and each pattern has yielded refinable data.

far in  $1/d$  spacing, they are better resolved and they do not have Ba fluorescence peaks from the glass capillary. Most importantly, the data can be refined; this is shown in Fig. 8 where the first phase of gypsum has been Rietveld refined. The unit-cell parameters agree

well with the literature,  $a = 1.05095(3)$ ,  $b = 1.52304(5)$ ,  $c = 0.653690(18)$  nm,  $\beta = 151.6320(11)$ ,  $\chi^2 = 3.6$ .

Fig. 9 shows three data sets selected from the 900 shown in Fig. 7(b). The phases have been superimposed and individually refined using the Pawley method. The phases are gypsum, bassanite and anhydrite. In the case of the middle phase, there is a coexistence of the first two phases that can be quantified by comparison of scale factors. The values of  $\chi^2$  for gypsum, bassanite and anhydrite are 3.69, 3.41 and 3.7, respectively. A multiphase Rietveld refinement using all 900 data sets has been undertaken and will be reported shortly.

### 3.4. SAXS/WAXS

The test SAXS data from a collagen standard are shown in Fig. 10. The data were collected in 1 s out to 30 orders of diffraction and a  $q$  value of  $0.03 \text{ nm}^{-1}$ . The first tests of the SAXS/WAXS combined experimental performance were carried out by analysing a 0.5% by weight high-density polymer (E76B38) in hexane. This experiment was designed to examine crystallization in constrained geometries. The block copolymer chains have two hydrophobic amorphous ends and a crystallizable centre. When the ethylene oxide crystallizes, the

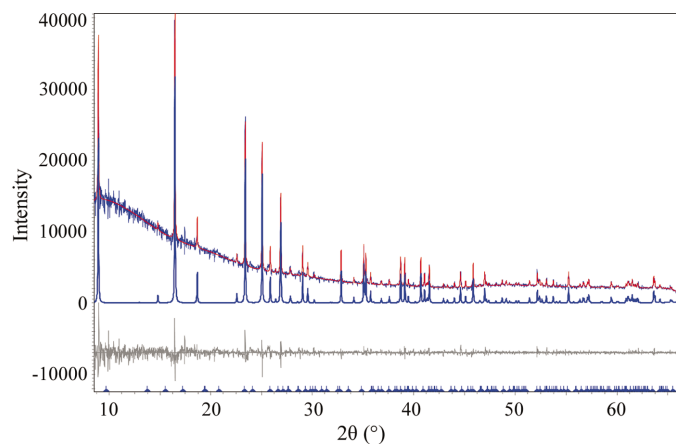


**Figure 8**  
A full Rietveld refinement of the gypsum data taken towards the start of the reaction process. The data were taken from the same experimental run shown in Fig. 7(b). The individual peak decomposition is shown in blue, the difference curve is shown in grey.

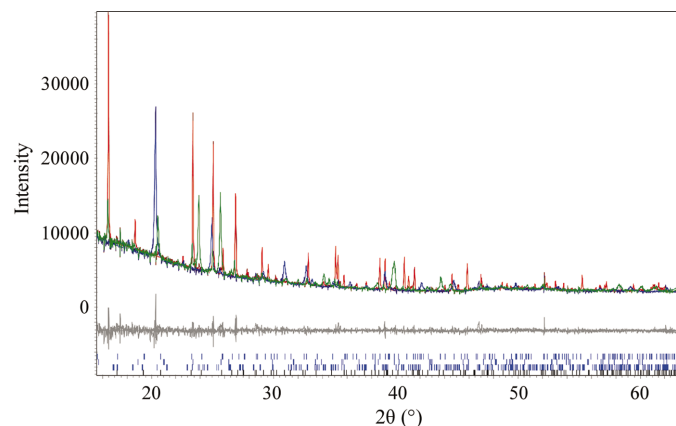


**Figure 9**  
Three data sets taken from the total reaction shown in Fig. 7(b). The data sets are from pure gypsum (refinement shown in Fig. 8), bassanite (with a little residual gypsum) and anhydrite. These data demonstrate that accurate cell refinements for quick phase identification can be obtained from the MPW6.2 data.

micelle ends up with exposed hydrophilic sides. A previous study on station 8.2 (Terrill *et al.*, 1998) showed that it was not possible to separate out the form and structure factor from those data since they were not of a sufficiently good statistical quality. The MPW6.2 data have subsequently been published by Heely *et al.* (2003). The small-angle-scattering data from a sample at 0.5 wt% enabled the form factor to be isolated providing information on the shape of individual micelles even at this very low concentration. The corresponding wide-angle-scattering data clearly show crystallization taking place within the micellar rafts at  $2\theta \gg 19.1$  and  $23.4^\circ$ , respectively. Crystallization at these low concentrations has not previously been observed.

### 3.5. XRD/XAS

A combined XRD and XAS measurement on the collapse and recrystallization of zinc-exchanged zeolite A (zeolite Zn/Na-A) was undertaken in order to benchmark the station performance in absorption spectroscopy. Previous studies of this material on station 9.3 at the SRS had been very successful as described in the *Introduction* and by Sankar *et al.* (1993). In order to investigate the performance of MPW6.2 we have repeated the experiment of Colyer *et al.* (1997) in which self-supporting disks of zeolite Zn/Na-A were heated in the DL/RI furnace (Dent *et al.*, 1995). Owing to constraints in the furnace geometry, only 1 mrad of horizontal flux was focused onto the sample, but the full vertical aperture of the beamline was utilized ( $\sim 2.4 \times 10^{12}$  photons  $\text{s}^{-1}$ ). XAS was measured in transmission using ion chambers that had a dilute Ar in He mix to avoid space-charge effects. Data were collected in step-scanning mode; 353 1 s data points were collected every 470 s. XRD was collected in 10 s steps using the RAPID2 detector described above at an energy below the Zn K edge to avoid a high background owing to fluorescence (9509 eV;  $1.3038 \text{ \AA}$ ). Thus XRD followed by XAS data were collected alternately every 480 s (8 min) as the temperature on the sample was ramped from 973 K to 1073 K at a rate of  $1 \text{ K min}^{-1}$ . Fig. 11(a) shows an XRD data set collected in 380 s (Colyer *et al.*, 1997) alongside data collected in 10 s on the new MPW6.2 beamline using the RAPID2 detector (Fig. 11b). It is clear that in terms of signal to noise the spectra are similar despite a difference in data-collection time of a factor of 38. Owing to the improved resolution of the new detector, the RAPID2 data also show a number of extra peaks. Fig. 12 shows the corresponding XAS spectra. The collapse of the zeolite at about 993 K is clearly seen as a density increase in the sample, leading to an increased absorption-edge jump. At this point the XRD shows the sample to be amorphous. Analysis of the XAS leads to the same

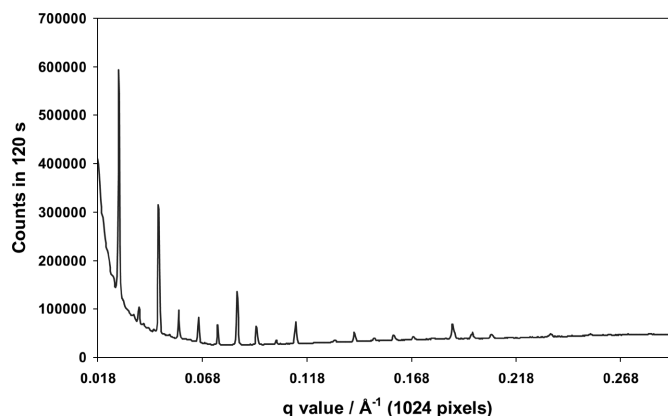


**Figure 10**  
Data taken from a collagen standard to test the performance of the SAXS detector. The data extend to 30 orders of diffraction.

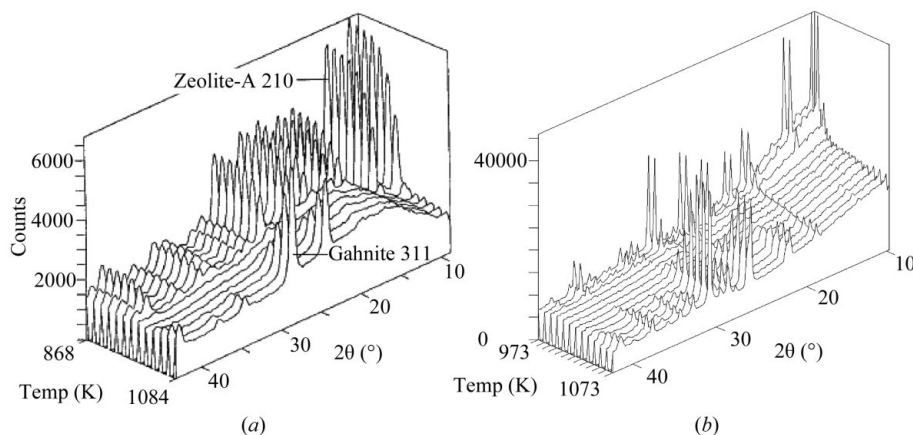


**Figure 11**

*In situ* combined XAS/XRD experiments following the heat treatment of Zn/Na-A. (a) XRD pattern from 868 to 1084 K (380 s measurement, station 9.3, INEL detector). [Reproduced from Colyer *et al.* (1997) with permission of the American Chemical Society.] (b) XRD pattern from 973 to 1073 K (10 s measurement, MPW6.2, RAPID2 detector).

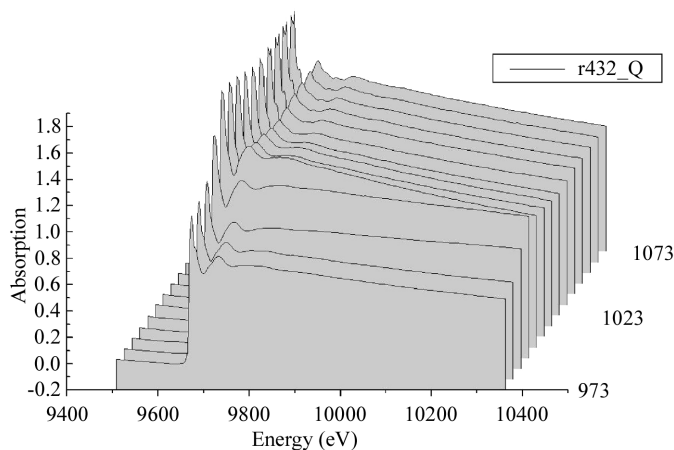


**Figure 12**

*In situ* XAS data following the heat treatment of Zn/Na-A. XAS pattern from 973 to 1073 K (470 s measurement).

conclusions as presented by Colyer *et al.* (1997), namely that the zinc in the starting hydrated material occupies a distorted octahedral coordination. At the point of collapse it becomes tetrahedral, but with substantial disorder in the nearest-neighbour O atoms. The material then crystallizes as  $\text{ZnAl}_2\text{O}_4$  (gahnite) as the temperature is increased.

#### 4. Conclusions

We have completed the build phase of a beamline to deliver a high X-ray flux in the energy range from 5 to 18 keV for the study of solid-state reactions and materials processing. We have demonstrated that the wide-angle (powder diffraction) data can be collected on the same time scale as the small-angle data and that the data are of refinable quality. Our test samples show that materials under realistic conditions of processing can yield suitable data for refinement on a 1 s time scale. We have also demonstrated that the high-resolution monochromatic data can be collected on the same time scale as the energy-dispersive data. This opens up new possibilities in the study of solid-state reactions to monitor physical variables while refining the atomic coordinates at each stage of the reaction.

The station has been designed with the stringent monochromator requirements of X-ray spectroscopy in mind, and data acquisition has been designed for all combinations of SAXS, WAXS and XAS within a single experiment. Combined XAS/XRD has been tested as described earlier. The measurements following the temperature-dependent collapse and recrystallization of Zn zeolite show that the resolution and speed is superior to data published by Colyer *et al.* (1997). They also show that data-collection-rate gains ( $\sim 40$ ) were achieved from this system. Since collecting these data the station focusing has been optimized and an extra factor of eight in flux has been achieved. We now consider that it will be possible to study zeolite amorphization from miniature specimens at heating rates exceeding

$100^\circ \text{ min}^{-1}$  and also recalescent re-crystallization in levitated super-cooled liquids that typically occur within tens of milliseconds.

The capability of the WAXS detector to collect refinable data has been illustrated using the well characterized dehydration sequence of gypsum ( $\text{CaSO}_4 \cdot 2\text{H}_2\text{O}$ )  $\rightarrow$  bassanite ( $\text{CaSO}_4 \cdot 0.5\text{H}_2\text{O}$ )  $\rightarrow$  anhydrite ( $\text{CaSO}_4$ ). The two transformations have been clearly resolved and the phases refined. These results demonstrate that high-resolution monochromatic data of refinable quality can now be collected on time scales faster than energy-dispersive methods.

Our SAXS/WAXS tests have now been published separately (Heely *et al.*, 2003). To our knowledge this is the first time that such a dilute polymer sample has been observed crystallizing from solution measured by a combination of small- and wide-angle scattering. The conditions surrounding the data collection were not ideal: only the central 1 mrad of beam was used because of time constraints. We therefore expect a factor of at least four in incident flux for future experiments. The SAXS and WAXS data are simultaneously collected by the RAPID2 data-acquisition system and time-stamped into the same data set. The data can be collected simultaneously up to the timing resolution of the system that is much faster than the data-collection times necessary for good counting statistics.

We are aware of two other facilities developing one-dimension fast-readout wide-angle detectors. These are the Dutch–Belgian beamline DUBBLE at ESRF (Borsboom *et al.*, 1998) and the materials science beamline at the Swiss Light Source (SLS) in Villigen (Fauth *et al.*, 2002), although the latter does not have a SAXS facility. Both facilities have taken a slightly different approach. The SLS are developing silicon solid-state detectors that can be tiled in arrays; these detectors are fast and have very high spatial resolution but suffer from poor efficiency above 30 keV and have little energy resolution. DUBBLE at ESRF have developed gas–glass microstrip technology in a curved linear detector. This is very fast but suffers from a lack of spatial resolution owing to the non-interpolating readout electronics. The RAPID2 development described in this paper compares very favourably with these developments. It has a better spatial resolution and better peak to background than DUBBLE and better energy resolution than the SLS silicon strip detector. However, there is a significant overhead in maintaining the RAPID detectors at their peak performance. We expect developments in the solid-state field to replace this type of gas detector in due course. However, the RAPID2 and SAXS detector combination represent a significant step forward in the development of equipment

to study changing structures under realistic and sometimes hostile processing environments. The station is now available for general use.

We are grateful to EPSRC for funding the beamline and the RAPID2 detector and to CLRC for providing the infrastructure and many of the project's technical, mechanical, computing, electrical and engineering staff. We would also like to thank the many Daresbury staff whose hard work and dedication ensured the success of the project.

### References

- Berry, A., Helsby, W. I., Parker, B. T., Hall, C. J., Buksh, P. A., Hill, A. T., Clague, N. J., Hillon, M., Corbett, G., Clifford, P. A., Tidbury, A., Lewis, R. A., Cernik, R. J., Barnes, P. & Derbyshire, G. E. (2003). *Nucl. Instrum. Methods Phys. Res. A*, **513**, 260–263.
- Borsboom, M., Bras, W., Cerjak, I., Detollenaere, D., van Loon, D. G., Goedtkindt, P., Konijnenburg, M., Lassing, P., Levine, Y. K., Munneke, B., Oversluizen, M., van Tol, R. & Vlieg, E. (1998). *J. Synchrotron Rad.* **5**, 518–520.
- Bowler, M., West, J. B., Quinn, F. M., Holland, D. M. P., Fell, B., Hatherly, P. A., Humphrey, I., Flavell, W. R. & Hamilton, B. (2002). *Surf. Rev. Lett.* **9**, 577–581.
- Cernik, R. J. (2004). In preparation.
- Cheung, K. C., Strange, R., Harvey, I., Dobson, B., Derbyshire, G., Kay, J., Binsted, N., Linford, R. & Hasnain, S. (1999). *J. Synchrotron Rad.* **6**, 161–163.
- Colston, S. L., Jacques, S. D. M., Barnes, P., Jupe, A. & Hall, C. (1998). *J. Synchrotron Rad.* **5**, 112–117.
- Colyer, L. M., Greaves, G. N., Carr, S. W. & Fox, K. K. (1997). *J. Phys. Chem. B*, **101**, 10105–10114.
- Couves, J. W., Thomas, J. M., Waller, D., Jones, R. H., Dent, A. J., Derbyshire, G. E. & Greaves, G. N. (1991). *Nature (London)*, **354**, 465–468.
- Dent, A. J., Greaves, G. N., Roberts, M. A., Sankar, G., Wright, P. A., Jones, R. H., Sheehy, M., Madill, D., Catlow, C. R. A., Thomas, J. M. & Rayment, T. (1995). *Nucl. Instrum. Methods Phys. Res. B*, **97**, 1–4; 20–22.
- Dobson *et al.* (2002). Internal Technical Memorandum. Daresbury Laboratory, Warrington WA4 4AD, UK.
- Duke, E. M. H., Kehoe, R. C., Rizkallah, P. J., Clarke, J. A. & Nave, C. (1998). *J. Synchrotron Rad.* **5**, 497–499.
- Fauth, F., Welte, J., Schmitt, B. & Patterson, B. D. (2002). *The powder diffraction end station at SLS*, [http://www1.psi.ch/www\\_sls\\_hn/](http://www1.psi.ch/www_sls_hn/).
- Heely, E. L., Maidens, A. V., Olmstead, O. P., Bras, W., Dolbnya, J. P. A., Terrill, N. J. & Ryan, A. J. (2003). *Macromolecules*, **36**, 3656–3665.
- Laundy *et al.* (1999). Internal Technical Memorandum. Daresbury Laboratory, Warrington WA4 4AD, UK.
- Masson, O., Dooryhee, E., Cheary, R. W. & Fitch, A. N. (2001). *Mater. Sci. Forum*, **378**, 300–305.
- Olmsted, P. D., Poon, W. C. K., McLeish, T. C. B., Terrill, N. J. & Ryan, A. J. (1998). *Phys. Rev. Lett.* **81**, 373–376.
- Sankar, G., Wright, P. A., Natarajan, S., Thomas, J. M., Greaves, G. N., Dent, A. J., Dobson, B. R., Ramsdale, C. A. & Jones, R. H. (1993). *J. Phys. Chem.* **97**, 9550–9554.
- Terrill, N. J., Fairclough, P. A., Towns-Andrews, E., Komanschek, B. U., Young, R. J. & Ryan, A. J. (1998). *Polymer*, **39**, 2381–2385.
- Wooster, W. A. (1936). *Z. Kristallogr.* **94**, 375–395.